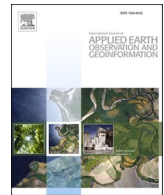




Contents lists available at ScienceDirect

International Journal of Applied Earth Observations and Geoinformation

journal homepage: www.elsevier.com/locate/jag



A multi-platform, open-source, and quantitative remote sensing framework for dam-related hazard investigation: Insights into the 2020 Sardoba dam collapse

Lei Xie ^a, Wenbin Xu ^{b,*}, Xiaoli Ding ^a, Roland Bürgmann ^c, Sanjay Giri ^d, Xiaoge Liu ^b

^a The Department of Land Surveying and Geo-Informatics, The Hong Kong Polytechnic University, Hong Kong, China

^b School of Geosciences and Info-physics, Central South University, China

^c Department of Earth and Planetary Science, University of California, Berkeley, CA, USA

^d Inland Water Systems Unit, Deltares, The Netherlands



ARTICLE INFO

Keywords:

Multi-platform and open-source data
Rapid hazard investigation
Remote sensing
Dam collapse
Dam deformation
Sardoba Dam

ABSTRACT

Monitoring dam deformation and reservoir conditions plays an important role in routine dam safety assessment. However, maintaining a real-time dam monitoring system and conducting frequent site surveys come with high costs, which may hinder the detection and mitigation of potentially hazardous dam conditions or incident investigations. In view of inaccessibility of *in situ* data for the scientific community and the need for rapid dam failure hazard investigation, we propose an end-to-end framework that relies on multiple and open-source remote sensing data for the dam-related hazard investigation (RSDHI). The proposed RSDHI framework includes three modules that are capable of monitoring the post-construction deformation status of the dam and the reservoir and provide the first-order and quantitative examination of the hazard causality based on numerical models. We apply and validate the RSDHI framework to a case study of the 2020 Sardoba dam failure in Uzbekistan. We show that the Sardoba Dam experienced continuing subsidence and a local ~ 4.7 cm differential settlement near the breached section. We reveal that the secondary consolidation controls post-construction deformation. The failure was likely related to the compound effect of transverse structural cracks that resulted from the differential settlement and water loading, yet the exact reason for its failure remains unknown. This study demonstrates that the RSDHI framework can combine multi-sensor remote sensing observations and numerical modeling to provide a complete and up-to-date status report of dam conditions, thereby providing insights into potential instability of dams around the world and enabling rapid investigation of their failures even when no *in situ* data is available.

1. Introduction

Dams and reservoirs provide significant social and economic benefits as they help to optimize water resource management and provide green energy production, but they also cause potential hazards and risks. In 2011, the International Commission on Large Dams (ICOLD) revealed that over 90% of dam failure events occurred on small dams (Pisaniello et al., 2015). In 2016–2020, most of the dam failure events occurred in case of earth-fill and low-head dams with less than ~ 30 m in height (Table S1). To identify the potential failure risk, effective structural monitoring is essential for both transient and progressive failures. However, ICOLD pointed out that most collapsed dams did not have effective structural surveillance or lacked appropriate monitoring

systems (Johansson, 1997). These recent catastrophic events and current operation scenarios pose the urgent demand for effective dam monitoring to deal with critical situations leading to hazards and losses and may provide early warning of impending failure.

Deformation of built structures is one of the main indicators of potential instability and plays an essential role throughout all stages of dam monitoring. Therefore, multiple on-site sensors (e.g., inclinometers, extensometers, and GNSS) are often installed on or inside dams to provide a reliable *in situ* system for structural integrity monitoring (Sciona et al., 2018). Along with the traditional ground-based and *in situ* observations, spaceborne remote sensing techniques, especially interferometric synthetic aperture radar (InSAR), have been shown to be capable of monitoring the stability of dams and surrounding infrastructures

* Corresponding author.

E-mail address: wenbin.xu@csu.edu.cn (W. Xu).

(Milillo et al., 2016). Compared with conventional methods, InSAR technology is independent of ground equipment and can be implemented at relatively low cost. Moreover, it can obtain spatially more extensive deformation fields (Grenerczy and Wegmüller, 2013; Wang et al., 2022).

The current space-based observations are typically coupled with other *in situ* data (e.g., water level, thermal and precipitation records) to analyze the correlation between deformation, hydrological conditions, and environmental factors (Milillo et al., 2016). Accurate characterization of the dam construction, materials, and geometry, as well as the underlying soil properties, are also relevant to quantify the deformation behavior, e.g., using finite element models (FEM) (Shamshiri et al., 2014). However, *in situ* dam monitoring data are not always easy to access for public use or studies by the scientific community. Particularly for older dams and embankments, the monitoring system is often not available.

The Sardoba Dam is located on the left bank of the Syr Darya river in

Uzbekistan. The natural landscape in the study area is a desert piedmont plain, namely “Hungry Steppe” (O’Hara, 2000). It is characterized by a continental and semi-arid to arid climate with an average temperature of $\sim 14^{\circ}\text{C}$ in the basin (Sorg et al., 2014). The precipitation in the Syr Darya basin is vertically zoned, with rainfall almost exclusively concentrated in the mountainous areas ($\sim 500\text{ mm/yr}$) and more arid conditions in the plain ($\sim 60\text{ mm/yr}$). During the 1960 s and 1970 s, the Soviet Union constructed a large irrigation system, including canals, reservoirs, and dams, to provide water in the Syr Darya river basin for the agriculture (Sorg et al., 2014). Since then, the desert lands have been transformed into irrigated agricultural areas for cotton and grain cultivation (O’Hara, 2000).

The Sardoba reservoir was designed for both irrigation and hydro-power purposes. The irrigation system of the reservoir is constructed based on the aging canal system-South Golodnaya Steppe (SGS) Canal (Rudnev and Umurzakov, 2018). The newly formed reservoir intercepts the water from the upstream Kairakkum reservoir, which improves the

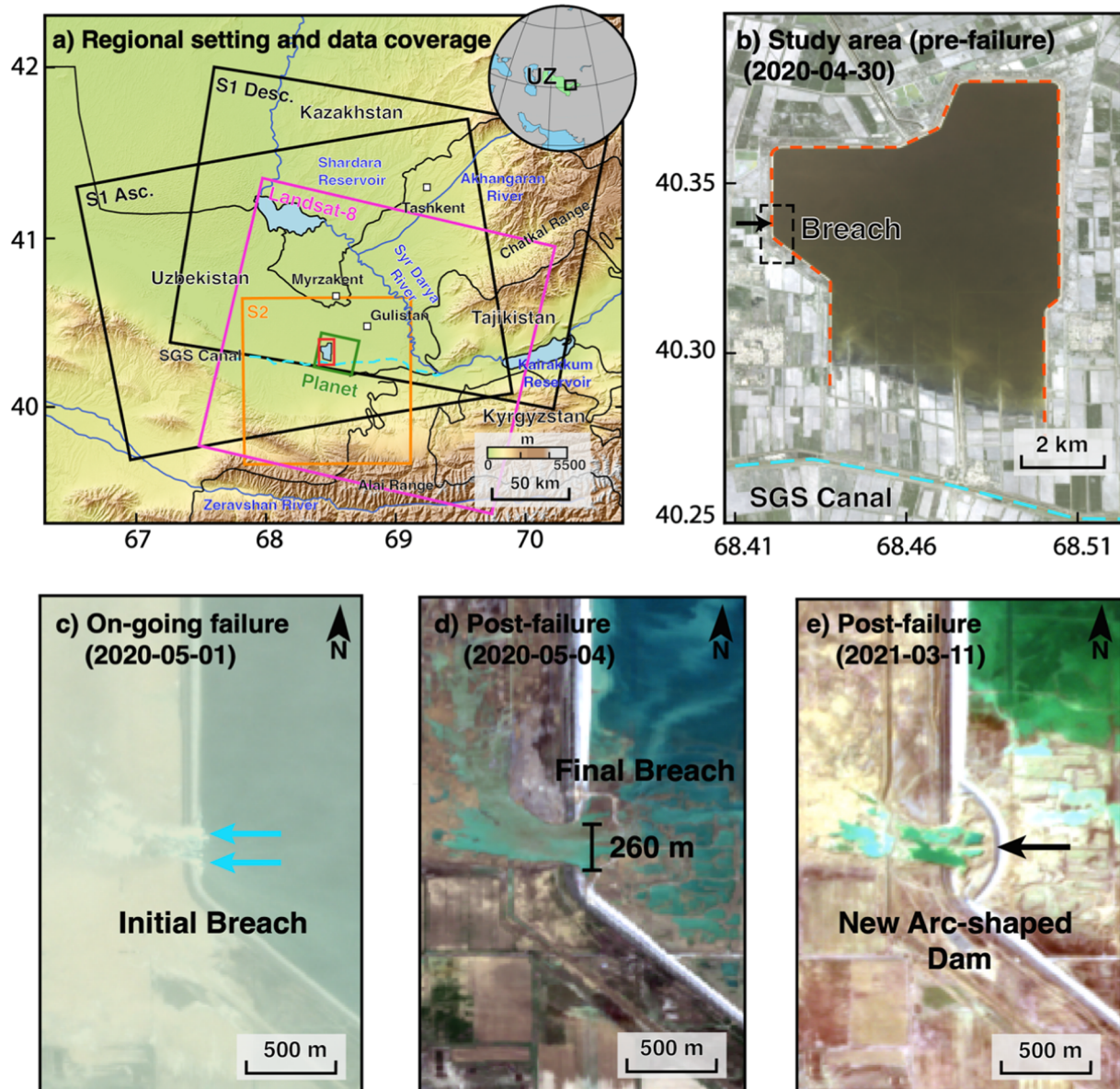


Fig. 1. Study area and satellite observations of the dam collapse. (a) The regional setting and data coverages. The black, magenta, orange, and green rectangles outline the frames of the Sentinel-1, Sentinel-2, Landsat-8, and the PlanetScope imagery, respectively. The red rectangle denotes our study area. (b) The status of reservoir one day before the collapse. (c) The enlarged view of the on-going failure (8:58 a.m., 1 May 2020). (d) The enlarged view after the dam collapse (4 May 2020). (e) Recent image from 11 March 2021 showing a newly built arc-shaped dam blocking off the breach.

water availability during the winter season in Uzbekistan. The Sardoba Dam is 28 km in length and up to 32 m height along its three sides (Fig. 1b, Rudnev and Umurzakov, 2018). This U-shaped earthen dam is filled with homogeneous compacted loam and silty loam. The whole works are laid on soft ground (i.e., a substrate of loess-like sediments and sandy loam) with a ~100 m loess-like loam and compacted sandy loam filled foundation. High-resolution satellite images show that the

northern and eastern sections of the dam already came into service at the beginning of 2014 (Fig. S1b). According to the water-spread area of the reservoir, the entire dam was put into tentative operation in May 2015 (Fig. S1e). At the breaking section, it is worth noting that the ancillary facilities (e.g., causeway and stone pitching) had not been completed until the early 2015 (Fig. S1g–h). The dam was officially commissioned in May 2017 after seven years of construction and created an

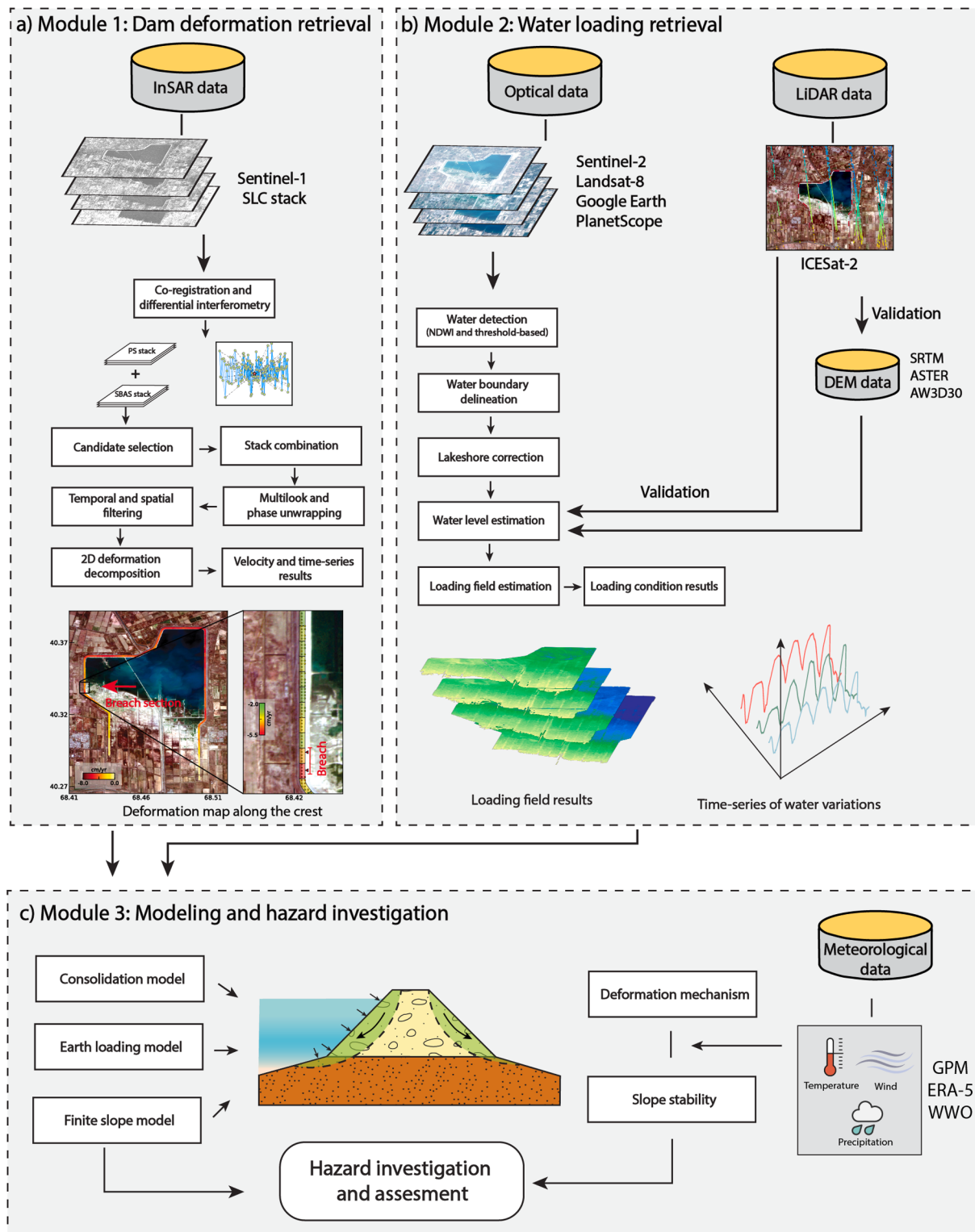


Fig. 2. Overview of the RSDHI framework: (a) dam deformation retrieval; (b) water loading retrieval; (c) modeling and hazard investigation based on remote sensing results.

impoundment that can hold as much as $0.92 \times 10^9 \text{ m}^3$.

On 1 May 2020 around local time 6:00 a.m. (UTC + 5), a catastrophic collapse occurred in a section of the Sardoba Dam following one week of heavy rainfall in the Syr Darya region, Uzbekistan (Fig. 1b). The breach is located near a bend along the western front of the dam, where the dam changes strike from $\sim 45^\circ\text{W}$ to $\sim 0^\circ\text{W}$ (Fig. 1). The evolving dam break resulted in two water outlets around 8:58 a.m. (Fig. 1c), and finally created a ~ 260 -meter-long breach section (Fig. 1d). The ensuing flood and associated mudflow caused six deaths, more than 50 injuries, and enforced at least 100,000 people in the Syr Darya river basin to evacuate (Xiao et al., 2022). Most of the reservoir volume capacity was depleted and the inundation spread further north to the southern territory of Kazakhstan, on 3 May 2020 (Giri et al., 2020). The economic losses amounted to about 1 billion US dollars, including the damages of households, infrastructures, and farmlands. Ten months after the incident, an arc-shaped replacement dam has been constructed to fix the breach (Fig. 1e).

Motivated by the problem of lack of *in situ* data and urgent need for rapid dam hazard investigation, we propose a new framework (namely RSDHI) that combines the multiple and publicly available remote sensing data (i.e., satellite radar, optical, and laser-ranging data) to track the hazardous dam-related events and investigate the possible dam failure causality. In the RSDHI framework, we establish several numerical models to explain the observed deformation and water variations. These remote sensing observations, numerical models in complement with other open-source data (i.e., DEM and meteorological data) can facilitate the dam deformation monitoring and dam-related hazard investigation in a rapid and quantitative manner. We apply this method to the 2020 Sardoba Dam collapse event in Uzbekistan. The results demonstrate the capabilities of the proposed framework and critical role of remote sensing in dam-related hazard investigation and can be easily extended to other dams, even without available *in situ* data; to improve our understanding of dam deformation in the post-construction period and facilitate the prevention of future tragic failures.

2. The RSDHI framework

2.1. Overview

The proposed framework aims to provide a remote-sensing based solution for the dam-related hazard investigation, featuring rapid response and quantitative evaluation. The proposed RSDHI framework includes three modules (Fig. 2): the first module is to retrieve ground deformation using satellite radar data; the second module is to calculate water loading of the reservoir from optical and LiDAR data; the third module deals with numerical modeling from remote sensing-based retrievals and dam-associated hazards.

2.2. Module 1: Dam deformation retrieval

We first selected the reference images and chose the image pairs to maximize their total coherence (Hooper et al., 2007). The stacks of SAR images were co-registered to the reference images using the InSAR Scientific Computing Environment (ISCE, Rosen et al., 2012). For both the ascending and descending data, we constituted two network configurations for creating the interferograms: a persistent scatterer (PS) network and a small baseline subset (SBAS) network at the full image resolution (e.g., Sentinel-1 in $\sim 5 \text{ m-by-20 m}$; Fig. S2). These two stacks of interferograms, making use of the different back-scattering properties of PS and distributed scatterer (DS) points, can improve the candidate scatterer density. Since the hydraulic infrastructures are generally stable scatterers, we used the amplitude dispersion (D_A) to select the coherent points with reliable targets as the candidate targets for the time-series analysis (Hooper et al., 2007). To keep the candidate targets on the breach section of dam crest, we only used amplitude dispersion from the

interferograms before the dam failure event. After the initial selection, band-pass filtering was employed on the wrapped phase to quantify the phase stability. We discarded the points when the resulting phase noise was greater than one overall phase-noise standard deviation. Subsequently, the different candidate points in the PS and SBAS stacks were combined to generate the single stack. To reduce the possible spatial aliasing and suppress the noise, we multi-looked and resampled the full resolution of interferograms into 30-by-30 m grids before the phase unwrapping procedure. Since the atmospheric screens are distributed randomly in temporal domain and smooth in the spatial domain, we used the conventional high-pass filtering in the temporal domain (i.e., 100 days) and low-pass filtering in the spatial domain (i.e., 150 m) to separate the atmospheric phase screens from the deformation signal (Li et al., 2022). Because of the near-polar orbits and oblique side-looking geometries of the SAR satellites, the sensitivity of InSAR measurement to the horizontal north–south motion is low. Therefore, we only decomposed the two-track LOS measurements into the vertical and east–west components (Fialko et al., 2001).

2.3. Module 2: Water loading retrieval

The water loading variations in the reservoir, including water level, water-spread area, and water volume, can be estimated and validated by optical image, LiDAR, and DEMs (Fig. 2b). The Normalized Difference Water Index (NDWI) makes use of the reflected near-infrared (NIR) band and visible green band (i.e., $NDWI = \frac{B_{Green} - B_{NIR}}{B_{Green} + B_{NIR}}$) and was used to detect the extent of surface water (McFEETERS, 1996). We applied the non-parametric segmentation method from Otsu (1979) to automatically determine the threshold in classifying water bodies from other land covers. We only kept the largest connected component to decrease the bias introduced by other water areas (e.g., paddy field, water channels, and rivers). Subsequently, we delineated the water boundary based on the extracted water extent to represent the varying water occurrence of the reservoir.

Since the construction of hydraulic engineering projects (e.g., dams and canals) and consequent impoundment (e.g., sediment and water) can modify the local topography, we evaluated the vertical accuracy of publicly available 30 m DEMs (Table S5), using LiDAR profiles acquired by the ICESat-2 data. The ICESat-2 ATL08 product (Level 3A) provides terrain height measurements at a meter-level accuracy (Neuenschwander and Pitts, 2019). A slope correction and best-fit terrain fitting polynomial terms were applied at the midpoint of each measuring segment. We only used the strong beams of ICESat-2 data which have higher SNR than the weak beams. We also filtered out the 20% of points that have the highest residuals between the measurements and referenced DEMs to avoid potential bias. The datum of the DEMs was converted to WGS-84 ellipsoid height to be consistent with the ICESat-2 products. Finally, all filtered ICESat-2 measurements can be used to select the DEM with the smallest vertical RMS in the research area.

With the delineated water boundaries and the selected DEM, we applied a DEM-based technique by averaging the elevations of the corresponding shoreline pixels (Park et al., 2020). To exclude the impact from the dam structure in which the shorelines are almost stationary, we set up a buffer area (i.e., 500 m) along the dam crest and only keep the shorelines outside in the buffer zone.

2.4. Module 3: Modeling and hazard investigation

According to the remote sensing retrievals of water loading fields and dam deformations, this module investigates the mechanism of dam deformation and the causality of dam failure through appropriate numerical models and meteorological data.

2.4.1. Investigation of deformation mechanism

2.4.1.1. Soil consolidation model. Since the progression of settlement is a key indicator for dam safety, we first examined the driving mechanism of the settlement along the Sardoba Dam. Theoretically, this time-dependent process, namely consolidation, reflects volume change of soil materials owing to the effective stress change (Tedd et al., 1997). According to the 1D Terzaghi's consolidation theory, the first phase of consolidation is the primary consolidation, in which the dissipation of excess pore pressure leads to an increase of effective stress. After that, when most (e.g., 95%) of the excess pore pressure has been dissipated, the soil exhibits a secondary consolidation process (i.e., soil creep). Here, to validate the driving mechanism of settlement, an empirical model considering both the settlement velocity and dam's height, the settlement index (SI) model was applied based on Eq. (1) (Charles, 1986):

$$S_I = \frac{s}{1000 \times H \times \log\left(\frac{t_2}{t_1}\right)} \quad (1)$$

in which s is the settlement (i.e., vertical displacement, in millimeter) from time t_1 to t_2 , and H represents the height of the dam (in meter). Typically, when the dimensionless SI is less than 0.02, it represents deformation controlled by secondary consolidation (i.e., a creep process), in which grain-to-grain rearrangement is continuous (Tedd et al., 1997). As we do not know the details of the dam construction and consolidation history (e.g., timeline for filling the placement in each stage and materials), we cannot establish an accurate mechanical model to fit the observation data (Shamshiri et al., 2014). Thus, we employed a simple analytical expression of an exponential settlement model, based on Terzaghi's 1D consolidation theory to express and predict the retrieved settlements (Yao et al., 2018). The exponential model can be expressed as:

$$S = S_\infty (1 - \alpha e^{-\beta t}) \quad (2)$$

in which S is the settlement value from InSAR observations, S_∞ is the final settlement, and α and β are two parameters to represent the exponential relationship.

2.4.1.2. Earth loading model. The dramatic water mass reduction after the dam failure may result in crustal elastic rebound, which has been observed in several reservoirs (Xie et al., 2021). We used a layered earth loading model based on Preliminary Reference Earth Model to simulate the crustal uplift after the water removal (Farrell, 1972). The corresponding loading Green's functions in the horizontal direction u_θ and the vertical direction v_θ are:

$$\begin{aligned} u_\theta &= \frac{a}{m_e} \sum_{n=0}^{\infty} h'_n P_n(\cos\theta) \\ v_\theta &= \frac{a}{m_e} \sum_{n=1}^{\infty} l'_n \frac{\partial P_n(\cos\theta)}{\partial\theta} \end{aligned} \quad (3)$$

where m_e , a , P_n , ∂P_n , and θ are the mass of Earth, radius of Earth, Legendre polynomials of the harmonic degree n , the partial derivative of the Legendre polynomials, and angular distances between the loading (i.e., water loading in reservoir) and the target point (i.e., near-field lakeshore), respectively; and h'_n and l'_n are the load Love numbers, which represent the horizontal and vertical surface responses, respectively.

2.4.1.3. Seasonal factors. By consideration of soil consolidation and crust response, the remainder of dam deformation is related to the seasonal factors. The elastic deformation and volume change due to shrink and swell effects is subject to reservoir water variations. Similarly, the thermal expansion/contraction effect is also with respect to the regional temperature changes. Therefore, if seasonal factors such as

water cycles and temperature impact or control the settlement on the crest, the deformation signals should exhibit periodic variations. Therefore, we cross-correlated the time-series of seasonal factors with the decomposed InSAR time-series. To exclude the impact of consolidation, the settlement (vertical subsidence) is detrended using the exponential models (Eq. (2)).

2.4.2. Investigation of slope stability

To characterize the impact from the cycle of water loading (i.e., external forces) on the dam, we used a finite element model to quantify the slope stability due to the change of water loading conditions with GeoStudio software (Geo-Slope International Ltd., 2012). The SLOPE/W and SEEP/W modules of GeoStudio were used to develop a 2D coupled model to estimate the contributions from two physical processes: the direct water loading (i.e., hydrostatic pressure increases) and the following seepage force (i.e., dissipation of excess pore pressure under the transient state) on the dam. The limit equilibrium approach was applied to quantify the slope stability by dividing the slope into small slices and solving the force equilibrium condition to obtain the driving force and resisting force acting on the critical slope plane. Using the factor of safety (FS, the ratio for the shear strength and acting shear stress) as the indicator, we can determine the critical slip surfaces and the stability changes of both up-stream and down-stream slopes.

3. Application to the 2020 Sardoba dam failure event

3.1. Description of dataset

We employed SAR acquisitions from two Sentinel-1 orbits to map the spatiotemporal deformation of the dam during the post-construction period (May 2015–December 2020). Owing to the spatio-temporally variable cloud coverage, we selected Landsat-8 (April 2015–May 2017), Sentinel-2 (September 2015–January 2021), and PlanetScope (April 30, 2020) images to retrieve the water surface changes (Fig. 3 and Tables S2 and S4). By integrating the DEMs, we also estimated the water-level and storage variability of the reservoir. Google Earth (April 2015 and October 2016), Landsat-8 (December 2013–October 2014), and PlanetScope (November 2019–March 2021) images were used for visual inspection to determine the period of initial impoundment and the dam failure process. The ICESat-2 data (November 2018–August 2020) were used for validating the accuracy of the DEMs and water level estimates (Fig. 3 and Tables S4–S5). The wind speed from World Weather Online (WWO) (2010–2020), temperature from ERA-5 (2015–2020), and precipitation from WWO and Global Precipitation Measurement (GPM) (2010–2020) were used to examine the impact of meteorological effects on the Sardoba Dam.

3.2. Observations of dam deformation

The multi-temporal InSAR observations exhibit a well-constrained deformation of the peripheral U-shaped dam from May 2015 to December 2020 (Fig. 4 and Fig. S2). The warm colors indicate range increase along the satellite line-of-sight (LOS) direction, which reaches up to 5.8 cm/yr along the northern boundary of the dam. The neighboring infrastructures (e.g., roads, canals, and cities) are generally stable without displacement rates in excess ± 0.5 cm/yr. The ascending and descending velocity maps show a consistent deformation pattern throughout the dam (correlation at 0.91), which indicates that the ongoing deformation is predominantly in the vertical direction.

To outline the deformation along the crest of the dam, we averaged the point targets into 50-by-150 m grids along the dam crest (Fig. 5). Varying rates of subsidence were observed with an average of 3.2 cm/yr along the dam crest (Fig. 5a). The average rate of subsidence (4.5 cm/yr) on the northern side of the dam (C to F) is 1.6 cm/yr higher than along the neighboring N-S striking dam sections (B to C). The deformation near the breach section exhibits a differential settlement, which appears to be

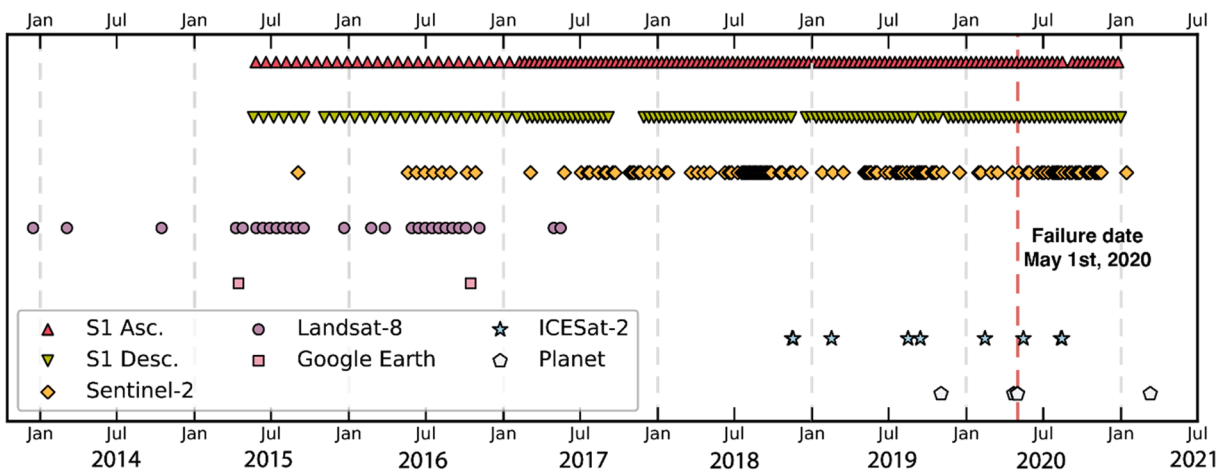


Fig. 3. The temporal distribution of satellite imagery used in the study: Sentinel-1 SAR ascending orbit (143 scenes), Sentinel-1 SAR descending orbit (133 scenes), Sentinel-2 optical (115 scenes), Landsat-8 (28 scenes), Google Earth image (2 scenes), ICESat-2 LiDAR (9 scenes), and PlanetScope imagery (6 scenes) (See Tables S3–4 for details).

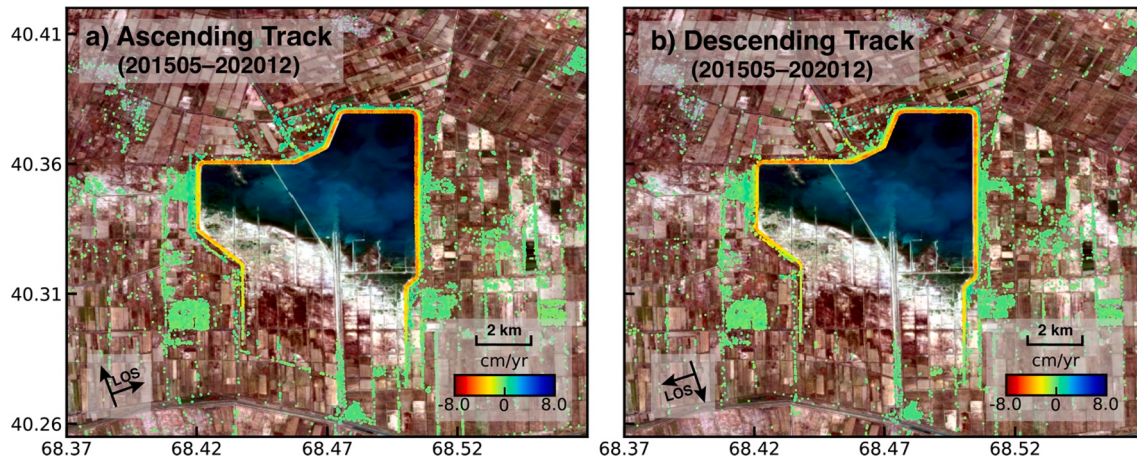


Fig. 4. The InSAR LOS deformation rate maps. (a) The surface displacement rate from ascending track (2015–05–26 to 2020–12–25), and (b) descending track (2015–05–20 to 2020–12–31).

divided by an underlying drainage canal (Fig. 5a). The neighboring grid point to the north of the drainage (i.e., G2) subsided at 5.0 ± 0.2 cm/yr, and the adjacent G3 at 4.2 ± 0.4 cm/yr. The cumulative 5-year differential settlement near the failure section (i.e., G2 to G3) reached 4.7 cm before the collapse. The horizontal rate map shows that most of the crest, including the breach section, did not experience resolvable east–west motion (less than 5 mm/yr, Fig. 5d–f). However, one 300 m length section along the northern embankment (near point D) and one 2.5 km length section (near point F) in the eastern part exhibit eastward motions at 1.5 cm/yr and 1.0 cm/yr, respectively (Fig. 5d).

We selected eight points across the dam crest that experienced different deformation rates (Fig. 5 points A–H for the locations). From the onset of our time-series observation, the widespread subsidence is developing linearly or quasi-linearly (i.e., rate reducing with the time) throughout dam (Fig. 6). The cumulative 5-year subsidence amounts to only 3 cm at the western end of the dam (point A) but reaches up to 35 cm near the northeast boundary (point F). Although horizontal east–west motion is insignificant in most regions of the dam, short sections of the dam near points D and F show eastward motions superimposed by the short-term fluctuations since January 2017. There is no evidence of precursory pre-collapse along the dam through two days before the dam collapse (i.e., ascending acquisition on 29 April 2020).

3.3. Estimates and verification of water variation

The AW3D30 DEM was used for water loading analysis considering its matches with the ICESat-2 data (Fig. S3). The retrieved water storage variations (i.e., water level, water surface area and reservoir volume) show a significant annual periodicity (Fig. 8). The average annual impounding amount is found to be about 0.5×10^9 m³. The first two impounding cycles (2015–2016) from before the completion of the dam show smaller annual storage gain (about 0.2×10^9 m³), while the later fill cycles (2017–2020) had higher amplitudes of about 0.7×10^9 m³. In 2020, the most recent cycle of water impoundment shows a maximum storage of about 0.76×10^9 m³ (from mid-October to end-April) in the reservoir. The day before the dam collapse, the water level and water-spread area were at 258.2 m and 54.5 km², respectively (Fig. 8). After the dam-collapse event, the reservoir lost about 76% of its maximum capacity (i.e., about 0.7×10^9 m³, Fig. 8b). Taking the ICESat-2 measurement on the water surface as a reference (2019–02–16: 255.9 m, 2020–02–14: 255.3 m, 2020–08–14: 239.6 m), the corresponding water level estimates using the AW3D30 DEM also show a small difference at 0.4 m (Fig. S3).

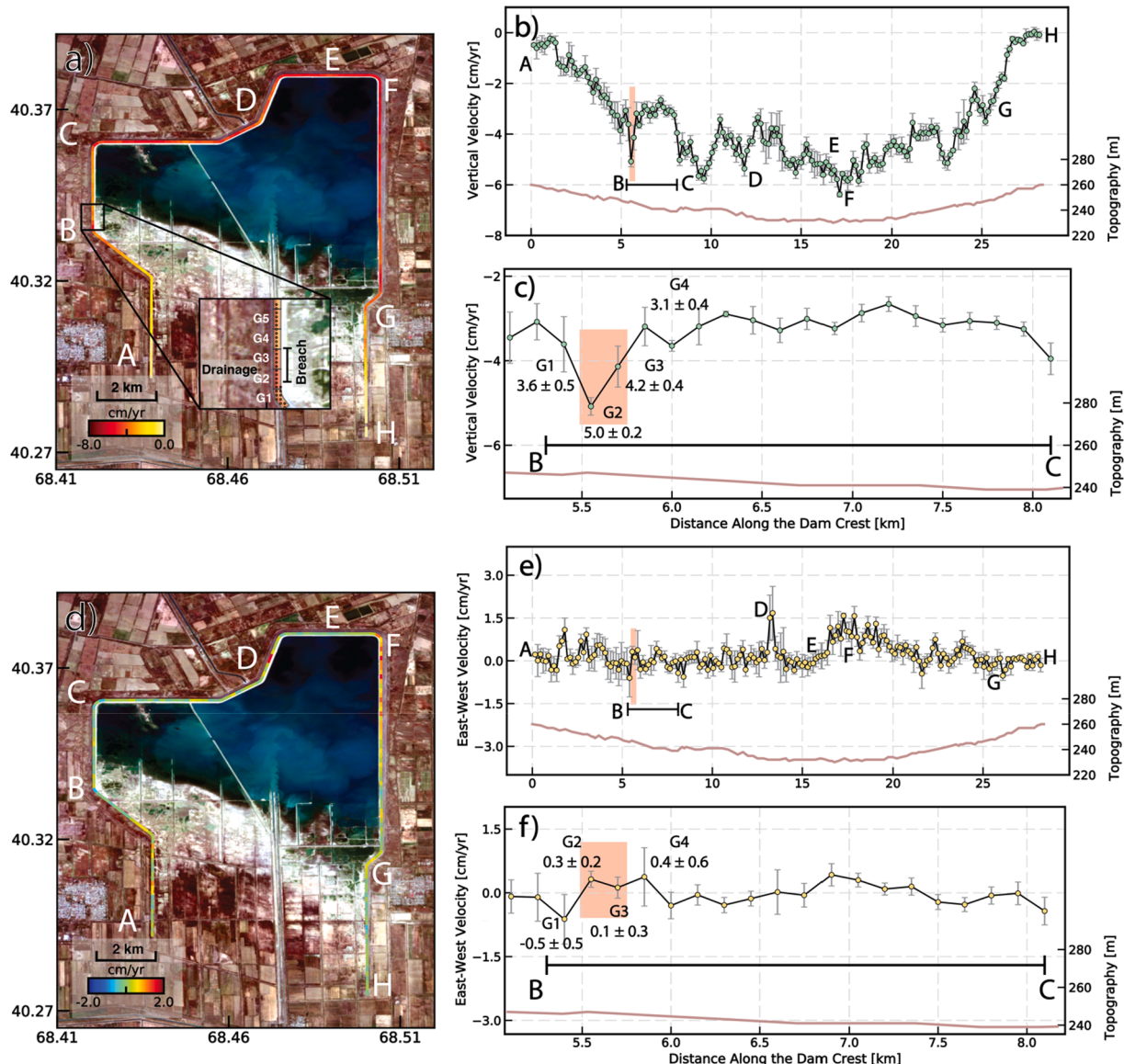


Fig. 5. The vertical and horizontal east–west velocities along the crest of the dam. (a) the spatial distribution of vertical displacement rates. (b) The 2D profile of vertical velocity. (c) The enlarged view of the velocity profile from point B to C. G2 and G3 are the grid sections nearest to the final breach. (d)–(f) are similar to (a)–(c) but for east–west velocity.

3.4. The mechanism of dam subsidence

3.4.1. Results of consolidation modeling

In Sardoba Dam, we first examined the type of consolidation through the settlement index (i.e., Eq. (1)). We found that the estimated SI was less than the critical threshold 0.02 (Fig. 9), suggesting that the dominant mechanism of the settlement is the secondary consolidation. Therefore, considering the secondary consolidation is following the termination of primary consolidation, the dissipation of excessive pore pressure has almost been concluded. In addition, the comparison between typical short-term primary consolidation of the embankment and the long construction period in Sardoba Dam also supports our secondary consolidation model.

Second, we determined the amount of soil consolidation using InSAR time-series along the dam crest (i.e., Eq. (2)). The data from May 2015 to April 2020 were used for the nonlinear parametric fitting, and the remaining post-failure period (from May 2020 to December 2020) were used for validation (Fig. 10). In general, the predictions of the exponential model agreed well with the InSAR observations (Fig. 10b), which

exhibited a long-term decaying behavior and a total RMSE for 4.5 mm (Fig. 10c). The reliable performance of fitting and model prediction further suggested that the observed settlement signal derived from the InSAR time series was predominantly contributed by the secondary consolidation.

3.4.2. Results of unloading rebounds modeling

The Earth loading model prediction showed that there should be about 4–10 mm uplift, and a 1–2 mm outward horizontal deformation (Fig. 11a). However, the detrended settlement (i.e., residual between the settlement and exponential model) (Fig. 11b) and the east–west deformation (Fig. 11c) did not allow for resolving the model predicted motions. First, this may be related to the inaccurate 1D global elastic Earth structure employed in the model. The deformation response from the shallow crust is more sensitive to small surface load variations (less than 1 km^3) (Xie et al., 2021). Therefore, the local crustal structure may affect the modeled crustal response. Secondly, the low temporal resolution of the InSAR data may also limit the capability of extracting such transient, millimeter-level deformation. Thirdly, the crustal rebound may also be

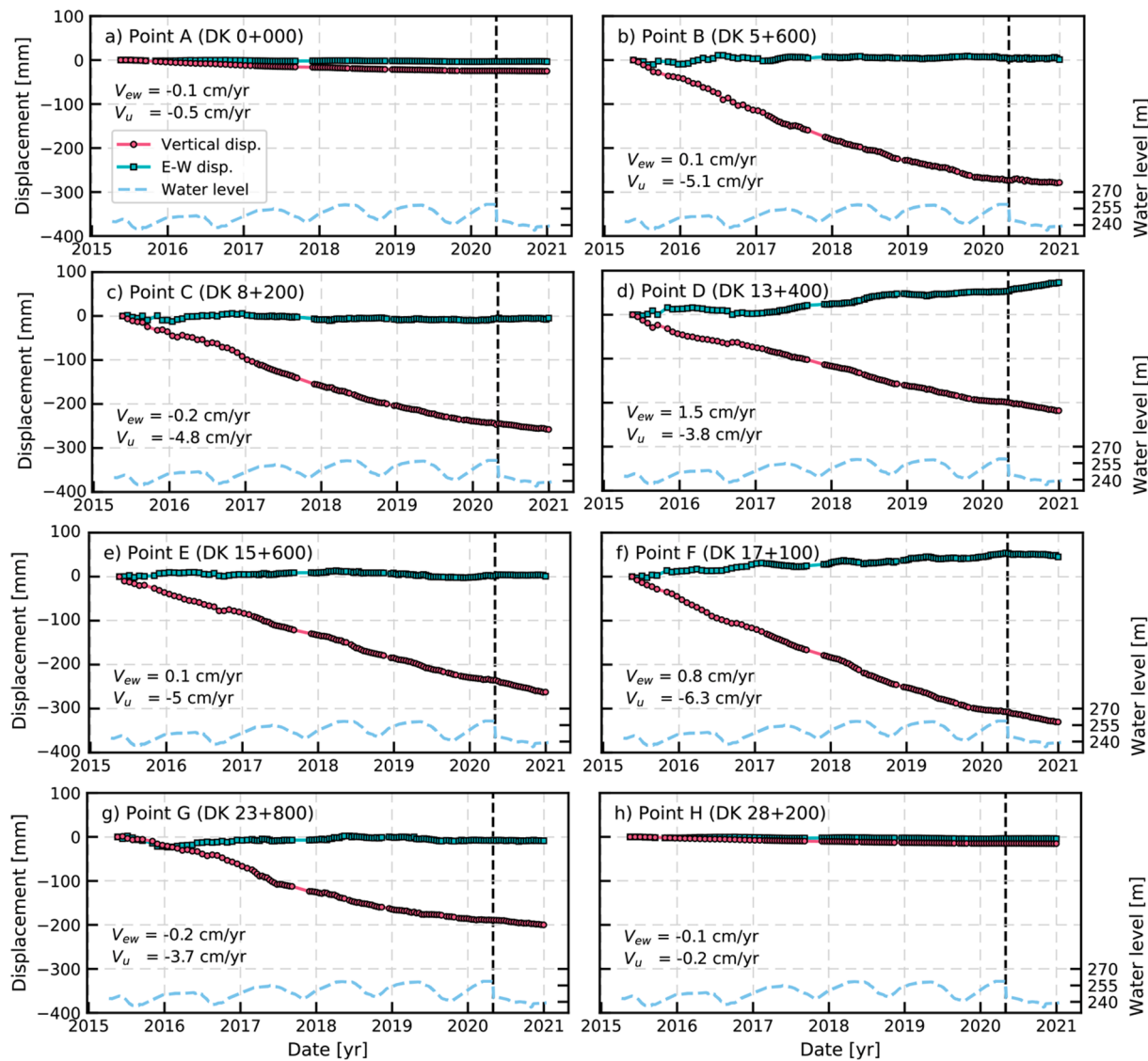


Fig. 6. The time series of cumulative displacement on the selected points A to H. The vertical deformation, east–west deformation, and the water level are depicted in red, cyan, and sky-blue, respectively.

affected by local hydrology (e.g., aquifer and groundwater) and the tectonic structure (e.g., local faults), therefore more *in situ* surveys may help to better explain the local crust behavior.

3.4.3. Impacts from seasonal factors

The seasonal variations of temperature and water level datasets suggested that both vertical and horizontal east–west displacements are not correlated with external fluctuations (Fig. 12). While the current observation and analysis provide no direct evidence of periodic deformation cycles, seasonal deformation may still occur on the earthen dam as millimeter-level fluctuations (Acosta et al., 2018). However, due to the lack of *in situ* observations and the moderate resolution of Sentinel-1 data, it is difficult to decipher the small seasonal deformation from thermal, elastic, and poro-elastic processes. We argued that the seasonal effects may contribute to the dam deformation but do not control the current motion of Sardoba Dam. High-resolution X-band SAR data (e.g., COSMO-SkyMed with $\sim 3\text{--}5 \text{ m}$ resolution) may help to capture and quantify the potential seasonal variation in the future.

3.5. Tests and results of slope stability

We put the water loadings fields from the recent mid-October to end-

April before the dam failure (i.e., water level 240.9–258.2 m) into the finite element model to evaluate the slope stability. We setup the model geometry according to the available cross-section with maximum height from Rudnev and Umurzakov (2018) (Fig. 13). The soil material of the dam was excavated from local loam deposits (i.e., sandy and silt loam). The raw material was rolled and compacted to the designed unit weight (i.e., $\gamma = 1650 \text{ kg/m}^3$) and then be homogenously filled to the dam. Except for the known unit weight of filling materials, we tested a range of loam materials based on laboratory experiments and other earthen dam failure events to quantify impacts of filling-materials on the slope stability (Gens and Alonso, 2006). Specifically, the selected effective soil cohesion (c') in the numerical simulation is 0–20 KPa, and the effective soil friction angle (ϕ') is 10–35°.

The time-series of FS on the up-stream slope showed an increasing tendency caused by 17.3-meter water loading before the dam failure event. For example, with effective cohesion $c' = 10 \text{ KPa}$ and effective friction angle $\phi' = 22.5^\circ$, the FS increased from 2.6 in October 2019 to 3.3 in April 2020 (Fig. 13a; Fig. S4). On the contrary, under the same dam material setting, the downstream slope showed an opposite tendency with FS from 3.1 to 2.4 during the recent water loading cycle (Fig. 13b; Fig. S5). The dam material testing also suggested a consistent result that the last loading cycle decreased the stability of the down-

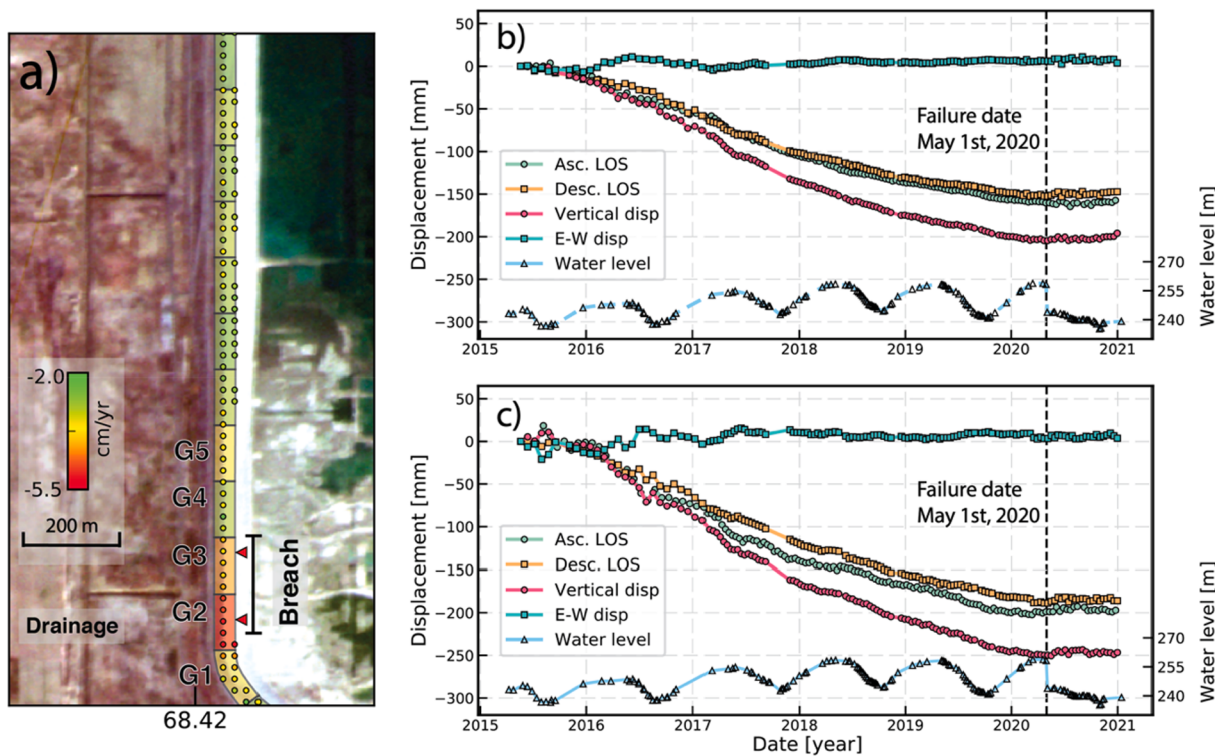


Fig. 7. The deformation rate and time-series near the breach. (a) The vertical deformation rate. Two red triangles show the locations of the initial breaches. (b) The time series of grid section around the northern breach. (c) The time-series of near the southern breaking point.

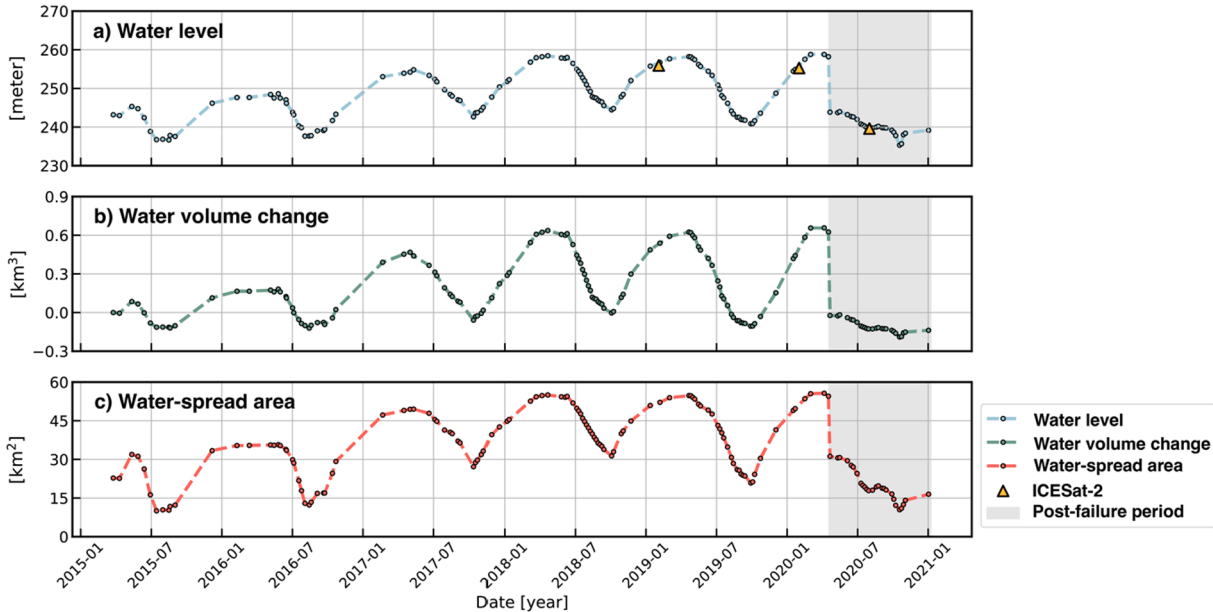


Fig. 8. The retrieved water variations in the Sardoba reservoir. (a) Water level. (b) Reservoir volume change. (c) Water-spread area. Three measurements from ICESat-2 are plotted as orange triangles (i.e., 2019-02-16, 2020-02-14, and 2020-08-14).

stream slope before the dam failure event (Figs. S4–S5).

4. Discussion

4.1. Differential settlement near the breach section

The InSAR analysis reveals a substantial differential settlement of up to 4.7 cm near the breach in the years prior to the failure date (i.e., G2 to

G3) (Fig. 14). This substantial differential settlement during the secondary consolidation period reflects potential defects in the underlying dam wall (the quality of construction) (Xiao et al., 2022). Considering the differential settlement between G2 and G3 (Fig. 7a and Fig. 14), transverse cracks (i.e., perpendicular to the crest) may have already developed near the breach section (Xiao et al., 2022). Such transverse cracks originating from differential settlement could have been further eroded by the water if the hydraulic shear stress is larger than the critical

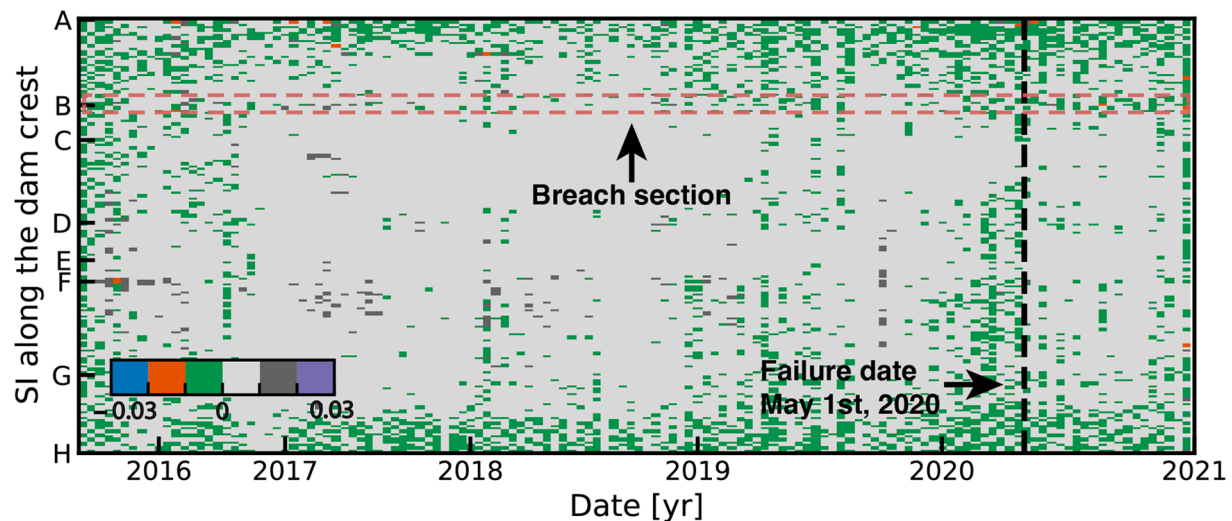


Fig. 9. The temporal evolution of the settlement index (Eq. (1)) on the dam crest. The SI for the grids along the crest.

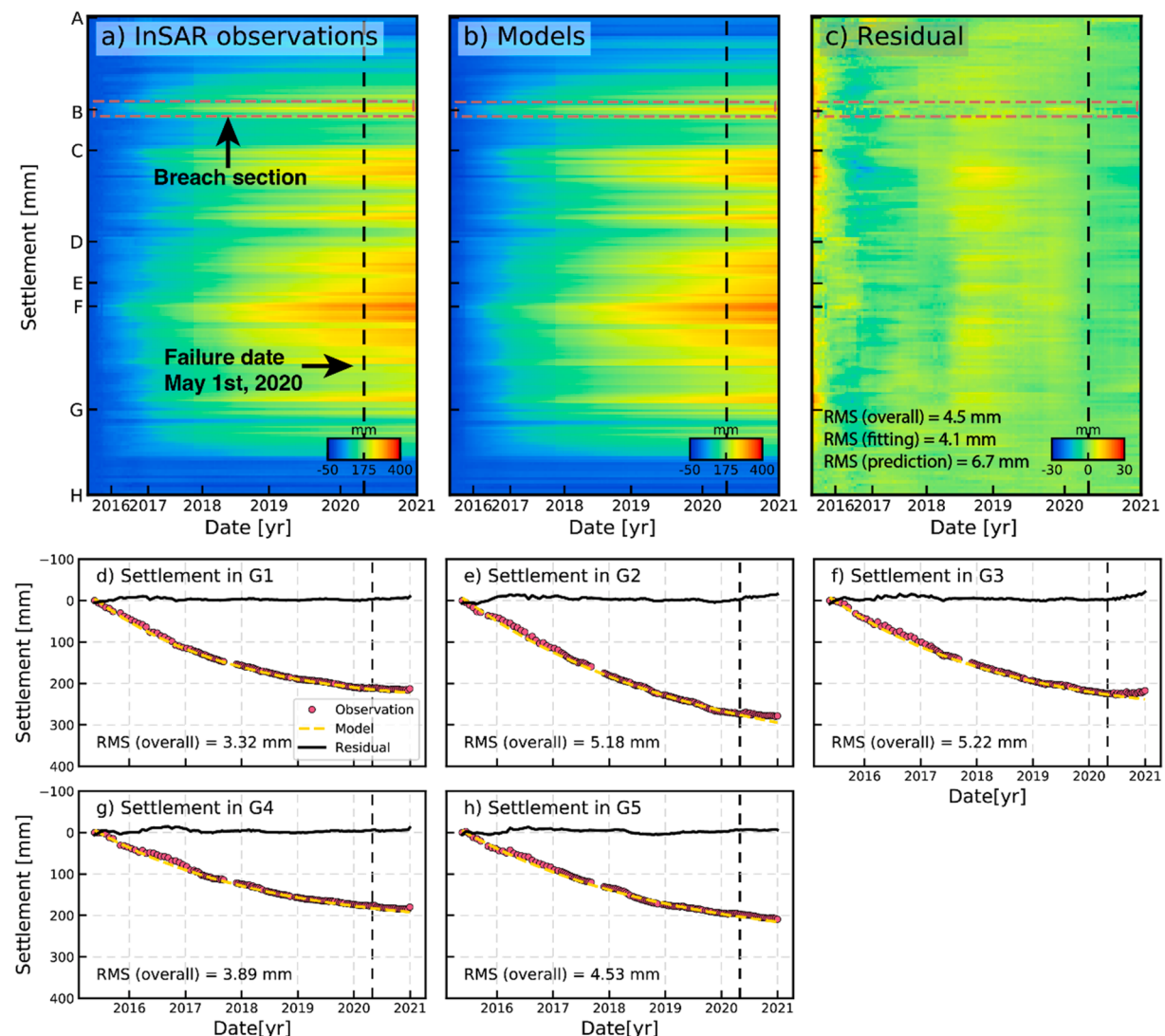


Fig. 10. The settlement observations and modeling results for the secondary consolidation. a)-c) The observation, model prediction, and residuals along the dam crest (sections A to H). d)-h) The time-series of selected grids G1–G5 near the breach section.

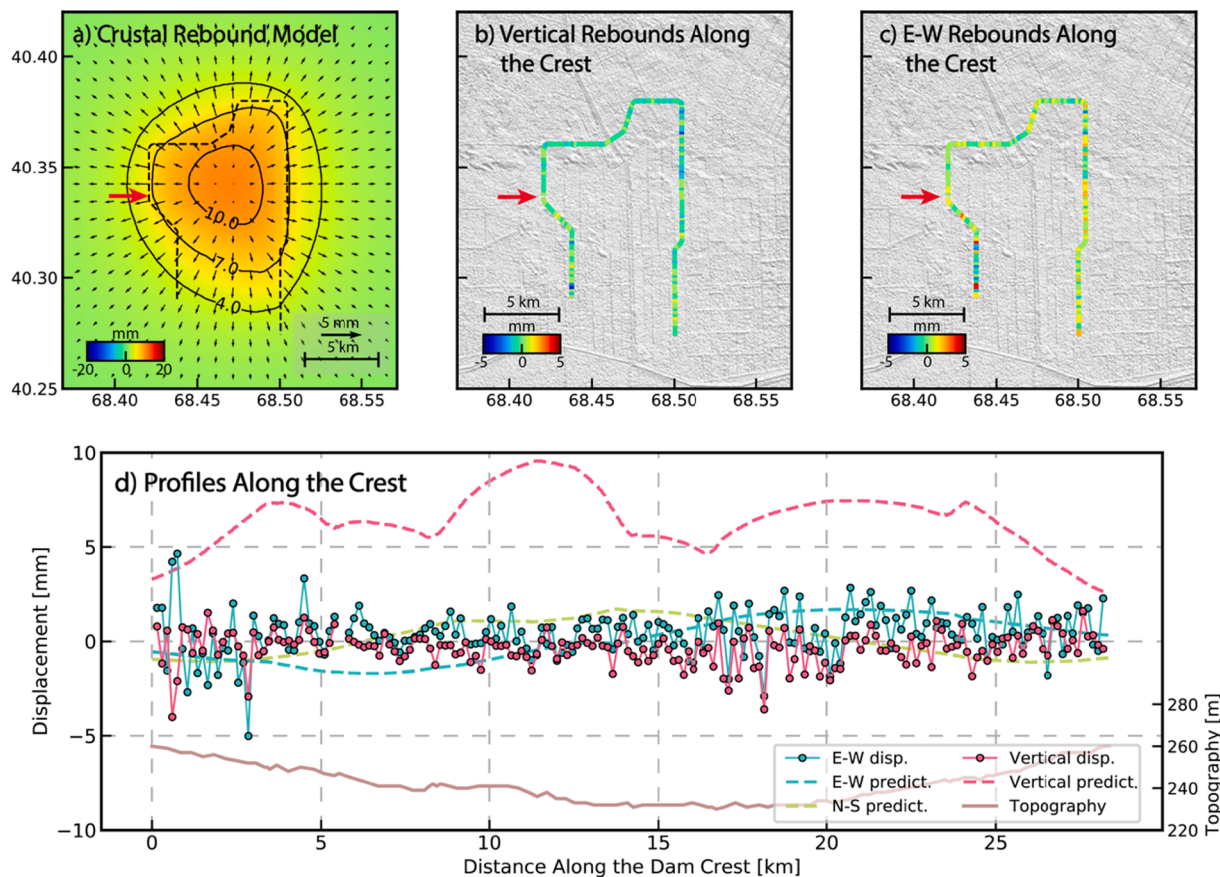


Fig. 11. The crustal rebound due to the water unloading from the dam failure. a) 3D deformation field from the elastic model. b) The observed vertical rebound. c) The observed horizontal east–west rebound. d) Profiles along the dam crest.

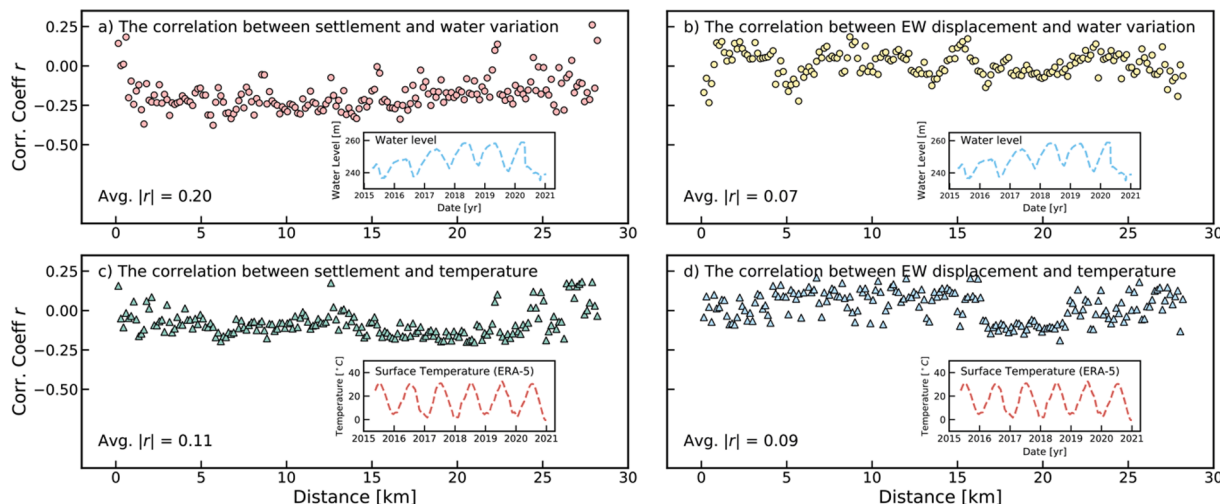


Fig. 12. The correlations between the settlement and seasonal factors. a)–b) The correlations between the water level and vertical and horizontal displacement, respectively. c)–d) Similar to the a)–b) but for the temperature variations.

shear stress of the filled materials. Subsequently, the developing cracks can form seepage paths allowing for piping initiation. Lessons from other earth-fill dam failure incidents such as the Apishapa earthen dam in Colorado (1923) and Stockton Creek Dam in California (1950) point to the dangers of transverse cracks from differential settlements, which may finally lead to the dam failure through piping (Getin et al., 2000).

4.2. Loading effect on the dam

While the $FS = 1$ is considered the critical condition in which the shear resistance is equal to the shear stress, we used FS values ranging from 1.3 to 1.5 because this represents a more practical ratio required for the slope stability (Ormann et al., 2013). In general, both slopes indicate downward motions with decreasing effective cohesion and effective friction angle. However, the obtained minimum FS values on

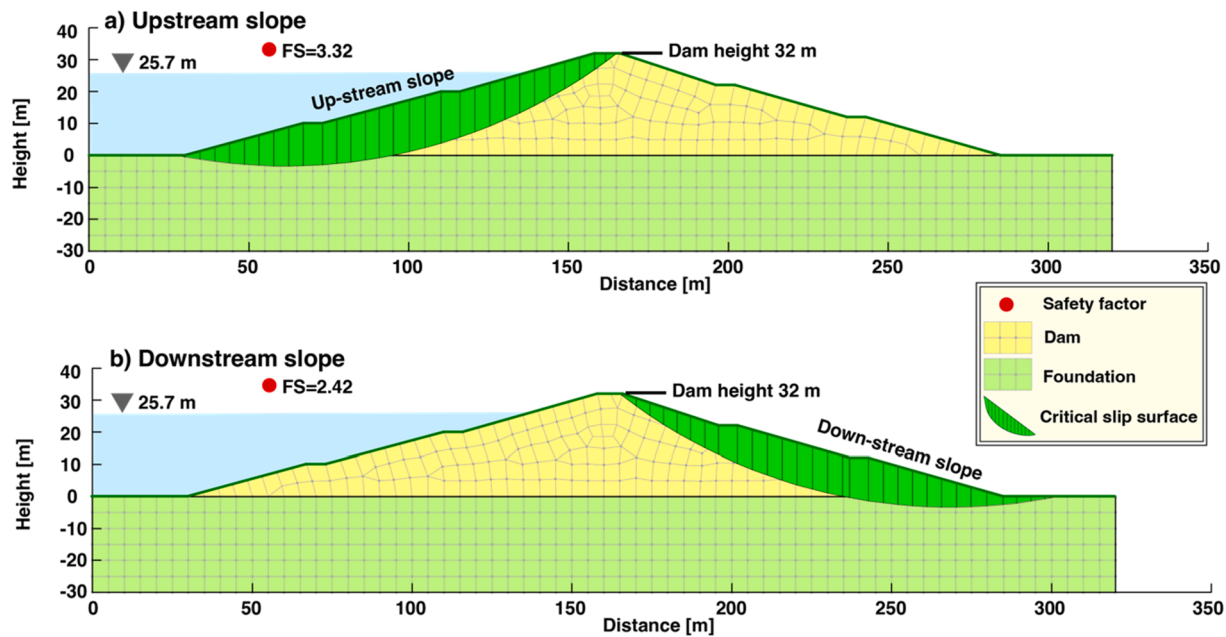


Fig. 13. An example for the critical slip surfaces (i.e., $c'=10$ KPa; $\varphi'=22.5^\circ$): a) Upstream slope. b) Downstream slope.

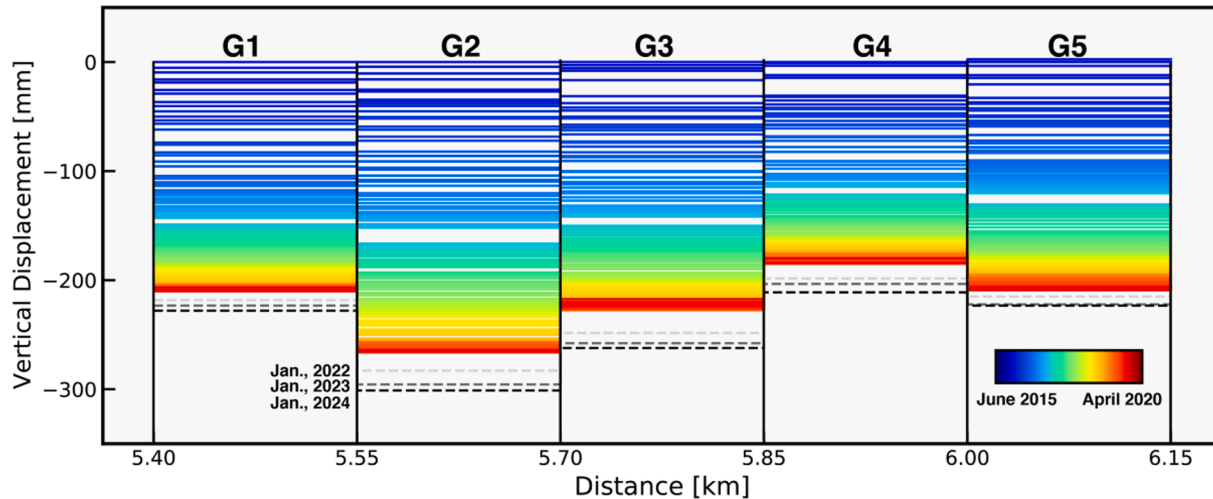


Fig. 14. The temporal evolutions of cumulative settlement near the breach section before the dam failure. The dashed lines indicate the expected future settlement (2022–2024) from the exponential model.

the upstream slope (1.68, Fig. S4c) and downstream slope (1.72, Fig. S5e) do not fall below the recommended safety threshold. While both of the slopes are stable during the recent loading cycle (i.e., FS greater than 1.5), the down-stream slope shows a decreasing factor of safety with the continuing loading (Fig. S5c–f). It indicates that the gradual rising of water level enhances the penetration of water into the dam body (Li et al., 2019). Consequently, the acting shear stress on the down-stream slope is increasing with the large pore pressure gradient. Therefore, before the dam failure, the slope stability of the down-stream is near the minimum point, which increases the risk of dam failure. Although our model may be biased due to the uncertainty from the accurate dam geometry and the actual material parameters, it still gives us a first-order estimation of slope stability evolution in the recent loading cycle.

4.3. Extreme hydrometeorological condition

Additional causes that have contributed to the dam failure may

include extreme hydrometeorological conditions (i.e., high precipitation and wind speed). Observations at the nearest meteorological station Yangiyer, located 27 km east of the reservoir, indicate following:

- On 28 April 2020, a maximum wind speed of 17 m/s was observed. No precipitation was observed on that day.
- A total rainfall of 45 mm was observed from 29 April to 30 April.
- No precipitation was observed from 30 April to 1 May. The maximum wind speed was 8 m/s. Prior to the failure, the wind speed was only 2 m/s.

As mentioned before, to complement the reported meteorological data, we used two datasets: 1) the weather models from WWO, which relies on global weather satellites and meteorological models to estimate hourly and daily climatological parameters (Fig. 15); 2) The precipitation data from the integrated multi-satellite retrievals of GPM were also considered for the comparison.

We found that both the Yangiyer station and the WWO data indicate

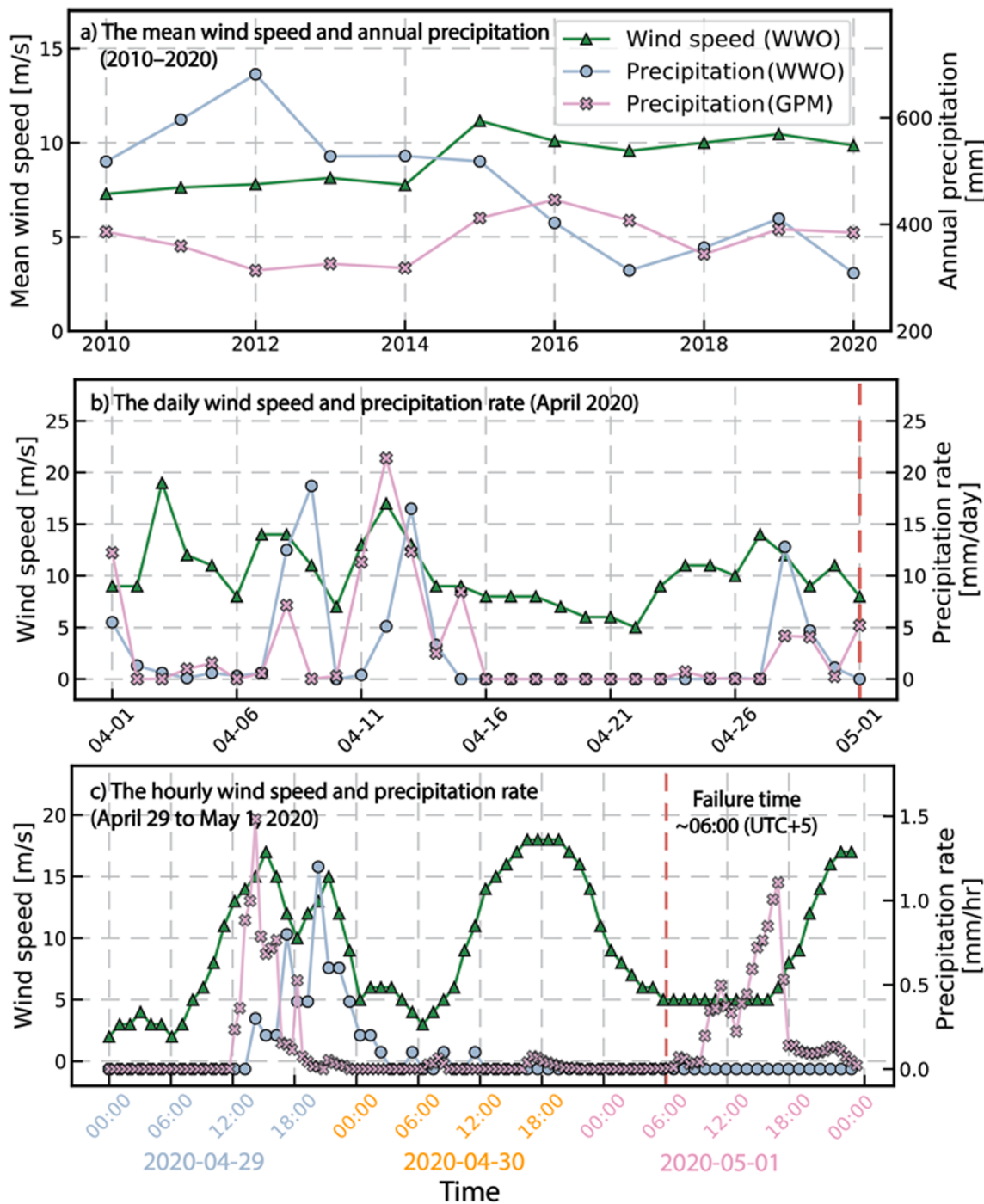


Fig. 15. Time series of rainfall and wind in the Sardoba area (40.2°N – 40.4°N , 68.4°E – 68.6°E). a) The average wind speed and annual precipitation. b) The daily precipitation and wind speed from April 2020 to May 2020. c) The hourly precipitation and wind speed before dam failure.

that there was mild-to-moderate wind speed (generally less than 10 m/s) before the dam failure (Table S6). On April 29, the amount of reported precipitation at Yangiyer station was as high as 45 mm/day, which was accounting for ten percent of annual precipitation (Fig. 15b). However, all three independent datasets showed that there was insignificant rainfall in the final day before the dam failure (April 30, Fig. 15b). The inflow into the reservoir is through a canal whose discharge can be controlled; i.e., the reservoir is not in a river system that should not be affected by large river discharge. This may imply that the hydrological factors were less likely to be the cause of the failure.

5. Conclusions

In this paper, we proposed a new remote sensing-based framework (RSDHI) to investigate the dam-related hazards, aiming to cover the shortage of *in situ* data and provide a rapid and quantitative investigation of dam failure events. We applied the proposed method to map the evolution of post-construction settlement of the U-shaped Sardoba Dam, an earth dam in Uzbekistan, to retrieve the water variation in the dam, and to investigate the possible factors leading to the dam failure. We found that significant settlement at a maximum rate of 6.3 cm/yr occurred throughout the entire dam. Model calculations confirmed that secondary consolidation, rather than seasonal factors, controlled the

recent deformation of the dam. Our investigation showed that the observed ~ 4.7 cm differential settlement near the breach section may have played a role in the development of latent defects in the design and construction and transverse cracks in the dam body that may have led to the eventual collapse. We suggest such framework can be applied as a non-structural measure, viz. as a part of a regular monitoring and warning system for water infrastructures, to avoid sudden failures leading to disasters and fatalities.

Declaration of Competing Interest

The authors declare that they have no known competing financial interests or personal relationships that could have appeared to influence the work reported in this paper.

Acknowledgements

The research is supported by the National Natural Science Foundation of China under Grant (42174023), the Research Grants Council of the Hong Kong Special Administrative Region (PolyU 152233/19E), and Deltares' research program 'Natural Hazards'. All data used in this study are from public repositories.

Appendix A. Supplementary material

Supplementary data to this article can be found online at <https://doi.org/10.1016/j.jag.2022.102849>.

References

- Acosta, L.E., De Lacy, M., Ramos, M.I., Cano, J.P., Herrera, A.M., Avilés, M., Gil, A.J., 2018. Displacements study of an earth fill dam based on high precision geodetic monitoring and numerical modeling. *Sensors* 18 (5), 1369.
- Cetin, H., Laman, M., Ertunc, A., 2000. Settlement and slaking problems in the world's fourth largest rock-fill dam, the Ataturk Dam in Turkey. *Eng. Geol.* 56 (3-4), 225–242.
- Charles, J.A., 1986. In: The significance of problems and remedial works at British earth dams. Institution of Civil Engineers, London, pp. 123–141.
- Farrell, W.E., 1972. Deformation of the Earth by surface loads. *Rev. Geophys.* 10 (3), 761–797.
- Fialko, Y., Simons, M., Agnew, D., 2001. The complete (3-D) surface displacement field in the epicentral area of the 1999 Mw7.1 Hector Mine earthquake, California, from space geodetic observations. *Geophys. Res. Lett.* 28 (16), 3063–3066.
- Gens, A., Alonso, E.E., 2006. Aznalcóllar dam failure. Part 2: Stability conditions and failure mechanism. *Géotechnique* 56 (3), 185–201.
- Geo-slope International Ltd., 2012. Slope/W. Slope stability analysis. GEOSLOPE International Ltd., Calgary, Alberta, Canada.
- Giri, S., Donchyts, G., Hegnauer, M., 2020. Rapid desk analysis of the dam breach at Sardoba reservoir in Uzbekistan. accessed 13 May 2022 Deltares. https://www.researchgate.net/publication/341326590_Rapid_desk_analysis_of_the_dam_breach_at_Sardoba_reservoir_in_Uzbekistan/citations.
- Grenerczy, G., Wegmüller, U., 2013. Deformation analysis of a burst red mud reservoir using combined descending and ascending pass ENVISAT ASAR data. *Nat. Hazards* 65 (3), 2205–2214.
- Hooper, A., Segall, P., Zebker, H., 2007. Persistent scatterer interferometric synthetic aperture radar for crustal deformation analysis, with application to Volcán Alcedo, Galápagos. *J. Geophys. Res. Solid Earth* 112 (B7), B07407.
- Li, Z., Ye, W., Marence, M., Bricker, J.D., 2019. Unsteady seepage behavior of an earthfill dam during drought-flood cycles. *Geosciences* 9 (1), 17.
- Li, S., Xu, W., Li, Z., 2022. Review of the SBAS InSAR Time-series algorithms, applications, and challenges. *Geod. Geodyn.* 13 (2), 114–126.
- Johansson, S., 1997. Seepage monitoring in embankment dams (Doctoral dissertation, Institutionen för anläggning och miljö). <https://www.diva-portal.org/smash/get/diva2:8066/FULLTEXT01.pdf> (accessed 2 April 2022).
- McFEETERS, S.K., 1996. The use of the Normalized Difference Water Index (NDWI) in the delineation of open water features. *Int. J. Remote Sens.* 17 (7), 1425–1432.
- Milillo, P., Perissin, D., Salzer, J.T., Lundgren, P., Lacava, G., Milillo, G., Serio, C., 2016. Monitoring dam structural health from space: Insights from novel InSAR techniques and multi-parametric modeling applied to the Pertusillo dam Basilicata, Italy. *Int. J. Appl. Earth Obs. Geoinf.* 52, 221–229.
- Neuenschwander, A., Pitts, K., 2019. The ATL08 land and vegetation product for the ICESat-2 Mission. *Remote Sens. Environ.* 221, 247–259.
- O'Hara, S.L., 2000. Lessons from the past: Water management in Central Asia. *Water Policy* 2 (4–5), 365–384.
- Ormann, L., Zardari, M.A., Mattsson, H., Bjelkevik, A., Knutson, S., 2013. Numerical analysis of strengthening by rockfill embankments on an upstream tailings dam. *Can. Geotech. J.* 50 (4), 391–399.
- Otsu, N., 1979. A threshold selection method from gray-level histograms. *IEEE Trans. Syst. Man Cybern. Syst.* 9 (1), 62–66.
- Park, E., Merino, E., W. Lewis, Q., O. Lindsey, E., Yang, X., 2020. A pathway to the automated global assessment of water level in reservoirs with synthetic aperture radar (SAR). *Remote Sens.* 12 (8), 1353. <https://doi.org/10.3390/rs12081353>.
- Pisanelli, J.D., Dam, T.T., Tingey-Holyoak, J.L., 2015. International small dam safety assurance policy benchmarks to avoid dam failure flood disasters in developing countries. *J. Hydrol.* 531, 1141–1153.
- Rosen, P. A., Gurrola, E., Sacco, G. F., & Zebker, H. (2012, April). The InSAR scientific computing environment. In EUSAR 2012; 9th European conference on synthetic aperture radar (pp. 730–733). VDE.
- Rudnev, S., Umurzakov, Z., 2018. Specific Issues of Construction of New Dams on Soft Grounds of Irrigated Lands in Uzbekistan. Foz do Iguaçu, Brazil: Third International Dam World Conference.
- Sciaioni, M., Marsella, M., Crosetto, M., Tornatore, V., Wang, J., 2018. Geodetic and remote-sensing sensors for dam deformation monitoring. *Sensors* 18 (11), 3682.
- Shamshiri, R., Motagh, M., Baes, M., Sharifi, M.A., 2014. Deformation analysis of the Lake Urmia causeway (LUC) embankments in northwest Iran: insights from multi-sensor interferometry synthetic aperture radar (InSAR) data and finite element modeling (FEM). *J. Geod.* 88 (12), 1171–1185.
- Sorg, A., Mosello, B., Shalpykova, G., Allan, A., Hill Clarvis, M., Stoffel, M., 2014. Coping with changing water resources: The case of the Syr Darya river basin in Central Asia. *Environ. Sci. Policy* 43, 68–77.
- Tedd, P., Charles, C.J.A., Holton, I.R., Robertshaw, A.C., 1997. The effect of reservoir drawdown and long-term consolidation on the deformation of old embankment dams. *Geotechnique* 47 (1), 33–48.
- Wang, C., Wang, X., Xu, Y., Zhang, B., Jiang, M.i., Xiong, S., Zhang, Q., Li, W., Li, Q., 2022. A new likelihood function for consistent phase series estimation in distributed scatterer interferometry. *IEEE Trans. Geosci. Remote Sens.* 60, 1–14.
- Xiao, R., Jiang, M., Li, Z., He, X., 2022. New insights into the 2020 Sardoba dam failure in Uzbekistan from Earth observation. *Int. J. Appl. Earth Obs. Geoinf.* 107, 102705. <https://doi.org/10.1016/j.jag.2022.102705>.
- Xie, L., Xu, W., Bürgmann, R., Ding, X., Gahalaut, V.K., Mondal, S., 2021. Tehri Reservoir Operation Modulates Seasonal Elastic Crustal Deformation in the Himalaya. *J. Geophys. Res. Solid Earth* 126 (8). <https://doi.org/10.1029/2020JB021122>.
- Yao, Y., Qi, S., Che, L., Chen, J., Han, L., Ma, X., 2018. Postconstruction settlement prediction of high embankment of silty clay at Chengde airport based on one-dimensional creep analytical method: case study. *Int. J. Geomech.* 18 (7), 05018004. [https://doi.org/10.1061/\(ASCE\)GM.1943-5622.0001191](https://doi.org/10.1061/(ASCE)GM.1943-5622.0001191).